



Forward and inverse diffraction in phasor fields

JORGE GARCIA-PUEYO*  AND ADOLFO MUÑOZ

Universidad de Zaragoza I3A, Zaragoza, Spain

*jorge.garciap@unizar.es

Abstract: Non-line-of-sight (NLOS) imaging is an inverse problem that consists of reconstructing a hidden scene out of the direct line-of-sight given the time-resolved light scattered back by the hidden scene on a relay wall. Phasor fields transform NLOS imaging into virtual LOS imaging by treating the relay wall as a secondary camera, which allows reconstruction of the hidden scene using a forward diffraction operator based on the Rayleigh-Sommerfeld diffraction (RSD) integral. In this work, we leverage the unitary property of the forward diffraction operator and the dual space it introduces, concepts already studied in inverse diffraction, to explain how phasor fields can be understood as an inverse diffraction method for solving the hidden object reconstruction, even though initially it might appear it is using a forward diffraction operator. We present two analogies, alternative to the classical virtual camera metaphor in phasor fields, to NLOS imaging, relating the relay wall either as a phase conjugator and a hologram recorder. Based on this, we express NLOS imaging as an inverse diffraction problem, which is ill-posed under general conditions, in a formulation named inverse phasor fields, that we solve numerically. This enables us to analyze which conditions make the NLOS problem formulated as inverse diffraction well-posed, and propose a new quality metric based on the matrix rank of the forward diffraction operator, which we relate to the Rayleigh criterion for lateral resolution of an imaging system already used in phasor fields.

© 2025 Optica Publishing Group under the terms of the [Optica Open Access Publishing Agreement](#)

1. Introduction

Non-line-of-sight (NLOS) imaging methods aim to reconstruct a hidden scene not directly visible from the observer's perspective. In this work, we focus on the particular case of active time-resolved NLOS imaging, which consists on illuminating a secondary visible surface (relay wall) with pulsed light and capturing the time-resolved light scattered back by the hidden scene onto the relay wall at picosecond resolution. Reconstruction methods are then used to invert the light propagation from the captured light signal and estimate the hidden scene. Otherwise said, given a forward model that describes how light propagates and interacts with the hidden scene until reaching the sensor, the reconstruction of this hidden scene can be seen as the inverse of such model.

Multiple methods for reconstructing NLOS scenes using time-resolved scattered light have been suggested, namely those based in backprojection [1–4], inverse methods [5], direct inversion of light transport [6] or wave-based approaches [7–9]. Phasor Fields is a wave-based reconstruction method that transforms the NLOS problem into a virtual line-of-sight (LOS) problem by treating the relay wall as a virtual camera [8]. It reconstructs the hidden object by propagating virtual light waves into the hidden scene, that is directly seen by this virtual camera. The propagation of virtual light waves is modeled with existing diffraction theory using the forward diffraction operator.

While current reconstruction methods provide reasonably accurate and clean hidden object reconstructions (solutions to the inverse problem), they do not come without limitations. There are limits on the resolution of the reconstruction coming from the boundary conditions of the capture at the relay wall, which, in the case of Phasor Fields, are explained by the Rayleigh Criterion [8,10]. There are also particular positions and orientations of objects within the hidden

scene that cannot be reconstructed, often explained as the missing cone [11,12]. Last, wave-based propagation methods can also generate out-of-focus or ringing artifacts when reconstructing at specific distances or using few virtual frequency samples. In this work, we further explore these limitations by delving deeper in the relationship between wave diffraction and NLOS imaging. From this deeper understanding, we reach the following contributions:

- We leverage the relationship between forward and inverse diffraction to answer why an inverse problem, such as reconstructing a hidden scene given the captured time-resolved indirect light on a relay wall, can be solved using a forward (diffraction) operator, as proposed in Phasor Fields (Section 4.1). This allows us to devise two new complementary perspectives on what the relay wall represents, a forward phase conjugator or a hologram recorder, in the computational domain of Phasor Fields.
- We present Inverse Phasor Fields, a new algorithm to reconstruct the hidden scene posing the NLOS imaging problem as an inverse diffraction problem that offers its own particular trade-offs between the reconstructed geometry and noise structure (Section 4.2).
- We propose a computable quality metric for hidden scene reconstructions, based on the matrix representation of wave propagation. We make the connection between this metric and the resolution estimator given by the Rayleigh criterion (Section 5).

2. Related work

Taxonomy of NLOS imaging techniques. NLOS imaging analyzes indirect illumination from light paths that have scattered one or multiple times in the hidden scene to reconstruct it. Depending on the nature of the emitter, we differentiate between active illumination, where a controllable light source is used to indirectly illuminate the hidden scene, or passive illumination, where ambient light or light emitted by the objects in the hidden scene is used. Depending on the captured measurements, we differentiate between time-resolved or steady-state. A more in-depth overview of NLOS setups and reconstruction methods is presented in recent surveys [13,14]. Here, we consider active time-resolved NLOS methods which consist on illuminating a relay wall with a light pulse and capturing the time-resolved illumination that arrives back to the sensor after having interacted with the hidden scene. The hidden scene is reconstructed using information about the time-of-flight of the photons.

Forward time-resolved light transport. The forward model (or image formation model) in active time-resolved NLOS imaging is based on time-resolved light transport and describes how light propagates from the emitter until it arrives back to the sensor. In the general case, the forward time-resolved light transport operator can be represented by the transient path integral [15] as the sum of all possible light paths of any length. When a pulse is emitted, the sensor captures a time-resolved signal, known as the impulse response function, that is described by this forward model. Although the impulse response function is usually measured and defined in time domain, it can also be directly captured and expressed in time-frequency domain [9]. Upon discretization, the image formation model can be expressed using the matrix form of the forward time-resolved light transport operator [5]. In Phasor Fields [8], the forward operator in time-frequency domain is applied for reconstructing the hidden scene, which is actually solving an inverse problem. In this work, we explore this apparent contradiction, of a forward propagator solving an inverse problem.

Inverse problem: active time-resolved NLOS. The inverse problem (or hidden scene reconstruction) consists on reconstructing the hidden scene given the captured impulse response function. The first reconstruction methods were based on ellipsoidal backprojection [1], which estimates the hidden-scene albedo values using the adjoint of the forward time-resolved light transport operator. In practice, the backprojection algorithm only accounts for three-bounce paths,

discarding higher-order bounce paths, and it is implemented by triangulating points according to the time-of-flight of the captured indirect light. Other approaches solve the inverse problem using inverse rendering algorithms (analysis-by-synthesis approach) [16], inverse methods [5,17] or a confocal capture system that allows expressing the forward model as a convolution so the estimation of the hidden scene becomes a deconvolution [6]. In contrast, Phasor Fields [8] imagines the hidden scene without explicitly inverting the forward problem, by introducing a virtual wavefield that is propagated by a diffraction operator. In our work, we explore how Phasor Fields solves the reconstruction problem without explicit inversion of the light transport, and propose a new method that explicitly inverts the forward-propagation Phasor-Fields operator.

Diffraction and lensless imaging. Diffraction is a fundamental phenomenon in wave optics, where light is represented as electromagnetic waves. It is key in several areas of optics and photonics, especially with the rapid development of state-of-the-art techniques based on wave propagation like computer generated holograms [18] or optical diffraction tomography [19]. Forward diffraction aims to obtain the output wavefield at a plane $z > 0$ given the input wavefield at a plane $z = 0$ and can be modeled by the scalar theory of diffraction. Different propagation methods exist to compute the output wavefield like Rayleigh-Sommerfeld diffraction (RSD), or approximations like Fresnel or Fraunhofer diffraction [10,20]. Inverse diffraction refers to the problem of recovering the input wavefield from the knowledge of the output wavefield [21–23]. It has many applications in modern optics where forward and backward propagation of waves are needed, like digital holography [24,25] or phase retrieval algorithms [26]. Coherent diffractive imaging [27,28] is a type of lensless technique for object reconstruction where an object is illuminated by a coherent light source and the diffraction pattern produced by the scattered light is recorded. The object is numerically reconstructed by propagating the recorded diffraction pattern with the wave propagation methods mentioned before. Recording of the phase of the diffraction pattern can be done by recording multiple diffraction patterns and using "phase retrieval" algorithms [29] or recording the interference with a reference wave using holographic techniques [30]. Coherent diffractive imaging can be performed with wavelengths ranging from X-rays [31] to THz [32]. In this work we leverage tools from diffraction into NLOS, as the Phasor-Fields forward propagator is the Rayleigh-Sommerfeld diffraction, which enables us to explore the role of the relay wall as different optical elements.

3. Background

In the following, we cover the background on the theory of forward diffraction (Section 3.1) and Phasor Fields (Section 3.2), which uses diffraction to reconstruct the hidden object in NLOS and it is the basis of our work. Then, we describe the theory of inverse diffraction and its relation with forward diffraction (Section 3.3). This establishes the basis that allows us to explain our contributions in Section 4: why Phasor Fields uses a forward operator to solve the inverse problem and our Inverse Phasor Fields NLOS reconstruction method.

3.1. Forward diffraction

Diffraction is the phenomenon where waves bend or spread as they encounter an obstacle or pass through an aperture, extending into the area that would typically be in shadow. In classical physics, this behavior is explained by the Huygens–Fresnel principle, which considers each point on a wavefront to act as a source of individual spherical wavefronts that interfere to form the observed diffraction pattern. In the case of two infinite planes, forward diffraction models the output wavefield $u_z(x, y)$ defined at plane $z > 0$, also known as sensor plane, given the input wavefield $u_0(x, y)$ defined at plane $z = 0$, also known as object plane (see Fig. 1(a) for an overview of the setup). Both object and sensor planes are considered to be infinite and continuous. Forward diffraction of a monochromatic wavefield with time-frequency ω is accurately modeled by the

Rayleigh-Sommerfeld diffraction (RSD) integral for each point (x, y) in the output wavefield as

$$u_z(x, y) = g_z(x, y) * u_0(x, y) = \int_X \int_Y g_z(x - x', y - y') u_0(x', y') dy' dx', \quad (1)$$

where $k = 2\pi/\lambda$ with $\lambda = c/\omega$ being the wavelength, c the speed of light and $g_z(x, y)$ is the forward diffraction kernel,

$$g_z(x, y) = \frac{z}{r} \frac{e^{ikr}}{r} \frac{1}{i\lambda} \quad (2)$$

with $r = \sqrt{x^2 + y^2 + z^2}$. Equation (1) can be expressed in spatial-frequency domain, where (f_x, f_y) are spatial frequencies, and $U_0(f_x, f_y)$, $U_z(f_x, f_y)$ and $G_z(f_x, f_y)$ are the 2D Fourier transforms of the input field $u_0(x, y)$, output field $u_z(x, y)$ and forward diffraction kernel $g_z(x, y)$ respectively. This formulation is known as the Angular Spectrum (AS) method [10],

$$U_z(f_x, f_y) = G_z(f_x, f_y) \cdot U_0(f_x, f_y), \quad (3)$$

and the forward diffraction kernel is

$$G_z(f_x, f_y) = e^{ikzm} \quad \text{with} \quad m = \begin{cases} \sqrt{1 - (\lambda f_x)^2 - (\lambda f_y)^2}, & (\lambda f_x)^2 + (\lambda f_y)^2 \leq 1 \\ i\sqrt{(\lambda f_x)^2 + (\lambda f_y)^2 - 1}, & (\lambda f_x)^2 + (\lambda f_y)^2 > 1 \end{cases}. \quad (4)$$

Usually, only homogeneous waves are considered, which are those with spatial frequencies with bandwidth that satisfy $(\lambda f_x)^2 + (\lambda f_y)^2 \leq 1$, and evanescent waves $(\lambda f_x)^2 + (\lambda f_y)^2 > 1$ are ignored because they decay exponentially within a few wavelengths of propagation distance z , making them negligible for most far-field diffraction and imaging applications. The cone-shape representation that partitions spatial frequencies into homogeneous and evanescent waves (Fig. 2) resembles the representation of spatial frequencies associated to surface orientations that lie in the missing cone in NLOS and can not be reconstructed [11], opening the possibility for a more exact analysis of feature visibility in NLOS including homogeneous and evanescent waves in the virtual domain.

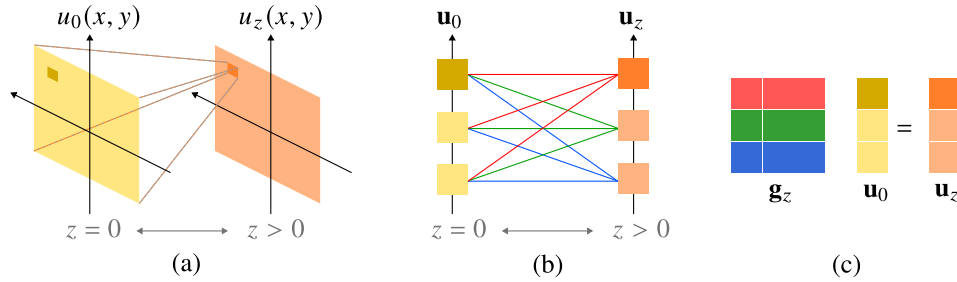


Fig. 1. (a) Wavefield propagation between input (object, $z = 0$) and output (sensor, $z > 0$) parallel planes, separated by z distance, using the forward wave diffraction operator $g_z(x, y)$. These planes are considered to be infinite and continuous. (b) Side view of the discrete propagation between input and output parallel planes, where each point (x, y) in the output wavefield is computed with information from all the points in the input wavefield. These planes are considered to be finite and discretely sampled. (c) Discrete plane-to-plane forward diffraction can be expressed as matrix-vector multiplication.

Forward diffraction with finite discrete apertures. When applying forward diffraction to real scenarios, additional considerations have to be made due to the finite and discretely sampled object and sensor planes of size $N_0 \times N_0$ and $N_z \times N_z$, respectively. These considerations change

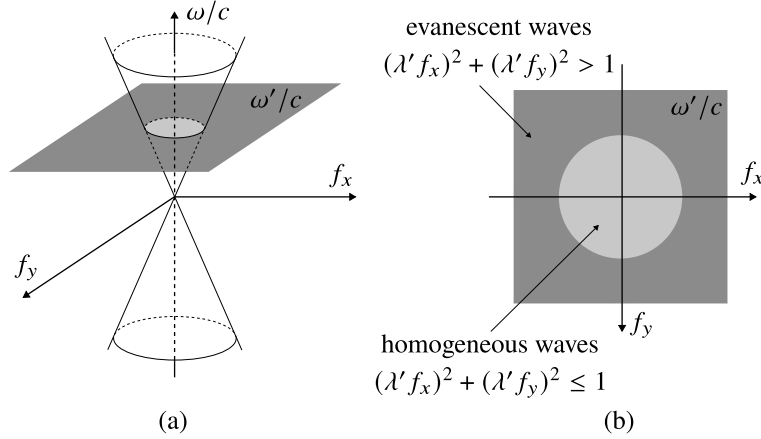


Fig. 2. (a) Spatial-frequency time-frequency domain is partitioned by a cone that splits the space between homogeneous (inside) and evanescent (outside) waves. The horizontal axes (f_x, f_y) represent spatial frequencies and the vertical axis (ω/c) represents time-frequency, adjusted to light speed c . Time-frequency axis can be also represented by inverse wavelength $1/\lambda = \omega/c$. (b) The spatial-frequency domain for a given time-frequency ω'/c (or the equivalent inverse wavelength $1/\lambda'$) is partitioned by a circle that splits homogeneous (inside) and evanescent (outside) waves.

the assumption of input and output planes being infinite and continuous, as stated in Eq. (1). Upon discretization, forward diffraction is expressed as a spatial-domain discrete convolution:

$$u_z[s, t] = \sum_{s'=0}^{N_0} \sum_{t'=0}^{N_0} g_z[s - s', t - t'] u_0[s', t']. \quad (5)$$

Alternatively, this convolution can be reformulated as a matrix-vector multiplication:

$$\mathbf{u}_z = \mathbf{g}_z \mathbf{u}_0 \quad (6)$$

where $\mathbf{u}_0 \in \mathbb{C}^{N_0^2}$, $\mathbf{u}_z \in \mathbb{C}^{N_z^2}$ and $\mathbf{g}_z \in \mathbb{C}^{N_z^2 \times N_0^2}$ with elements being formed from $g_z[s, t]$. This implicitly accounts for the summation over all points (x', y') on the input plane. Figure 1(b)-c show a side view of plane-to-plane forward diffraction expressed as a matrix-vector multiplication. Similarly, the diffraction model in the spatial-frequency domain can be discretized as an element-wise matrix-matrix multiplication:

$$\mathbf{U}_z = \mathbf{G}_z \cdot \mathbf{U}_0 \quad (7)$$

where $\mathbf{U}_0, \mathbf{U}_z, \mathbf{G}_z \in \mathbb{C}^{M \times M}$, and M represents the number of spatial frequency samples in the discrete Fourier transform. The discrete forward diffraction model is used in Phasor Fields to propagate a virtual wavefield for imaging hidden objects.

3.2. Phasor fields

A classical active time-resolved NLOS imaging setup is composed of a laser at position \mathbf{l} and a sensor at position \mathbf{s} , both looking at the relay wall and without direct line-of-sight to the hidden scene which contains the hidden object. The scene's impulse response function is captured by illuminating points $\mathbf{x}_l \in \mathcal{L}$ on the relay wall with an ultra-short pulse $\delta(\mathbf{x}_l, t)$ (Fig. 3(a)). The sensor records the time-resolved indirect illumination at points $\mathbf{x}_s \in \mathcal{S}$, obtaining the impulse

response function of the hidden scene $H(\mathbf{x}_l, \mathbf{x}_s, t)$, where t represents time (Fig. 3(b)). The capture process of the impulse response function is common to all active time-resolved NLOS imaging methods.

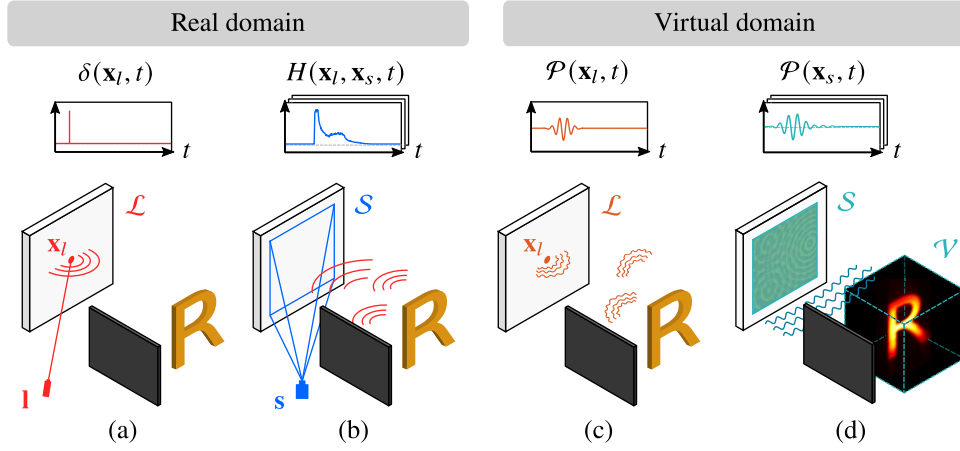


Fig. 3. Phasor Fields overview: (a) A laser l emits an ultra-short pulse of light $\delta(\mathbf{x}_l, t)$ illuminating points \mathbf{x}_l in the relay wall. (b) A sensor s captures the time-resolved indirect illumination defining the impulse response function of the hidden scene $H(\mathbf{x}_l, \mathbf{x}_s, t)$ at points $\mathbf{x}_s \in S$ on the relay wall. In the virtual domain, (c) the impulse response function $H(\mathbf{x}_l, \mathbf{x}_s, t)$ is convolved with an arbitrary pulse of illumination $\mathcal{P}(\mathbf{x}_l, t)$, obtaining the response wavefield $\mathcal{P}(\mathbf{x}_s, t)$ to that virtual illumination. (d) The relay wall becomes a virtual lens, and the response wavefield $\mathcal{P}(\mathbf{x}_s, t)$ is propagated to every point $\mathbf{x}_{v'} \in \mathcal{V}'$ using the RSD integral to compute the reconstructed wavefield $\mathcal{P}(\mathbf{x}_{v'}, t)$. *Figure inspired from Royo et al. [12].*

The novelty of Phasor Fields is the introduction of a virtual world where the relay wall acts as a virtual camera, converting the NLOS problem into a virtual LOS problem, enabling the application of known optics theory in the virtual world. The general idea is to virtually illuminate the hidden scene to compute a virtual image of the hidden scene under such illumination.

Virtual illumination of the hidden scene. In the real world, points \mathbf{x}_l in the relay wall reflect the light emitted by the laser. In the virtual world, these points \mathbf{x}_l become virtual emitters. From the impulse response function of the hidden scene $H(\mathbf{x}_l, \mathbf{x}_s, t)$, captured in the real domain using a delta illumination pulse $\delta(\mathbf{x}_l, t)$, we compute the virtual response that would be captured at the relay wall after illuminating the hidden scene with an arbitrary illumination $\mathcal{P}(\mathbf{x}_l, t)$ emitted virtually from $\mathbf{x}_l \in \mathcal{L}$. The result is the virtual response wavefield $\mathcal{P}(\mathbf{x}_s, t)$ at points $\mathbf{x}_s \in S$ in the relay wall, computed as

$$\mathcal{P}(\mathbf{x}_s, t) = \int_{\mathcal{L}} \mathcal{P}(\mathbf{x}_l, t) *_t H(\mathbf{x}_l, \mathbf{x}_s, t) d\mathbf{x}_l, \quad (8)$$

where $*_t$ is a convolution in time (Fig. 3(c)). Usually, the arbitrary illumination is defined as a Gaussian pulse in time-frequency domain. In Section 3.1, we defined the time-frequency ω and the wavelength λ of a wavefield. In this section, we will define the equivalent virtual time-frequency Ω and virtual wavelength λ_v for a wavefield in the virtual domain of Phasor Fields. The (virtual) time-frequency concept is different from spatial-frequencies (f_x, f_y) also defined in Section 3.1.

Virtual camera analogy. In the virtual world, the relay wall becomes a virtual sensor S composed of sensing points $\mathbf{x}_s \in S$ with direct line-of-sight to the hidden scene. The virtual image of the hidden scene is represented by the wavefield $\mathcal{P}(\mathbf{x}_{v'}, t)$ at points $\mathbf{x}_{v'} \in \mathcal{V}'$ in the

reconstruction volume. The reconstruction of the wavefield $\mathcal{P}(\mathbf{x}_{v'}, t)$ from a response wavefield $\mathcal{P}(\mathbf{x}_s, t)$ is a problem already solved in optics using wave-based imaging operators in time-frequency domain. We express the response and reconstructed wavefields in time-frequency domain applying the Fourier transform with respect to time, $\hat{\mathcal{P}}(\mathbf{x}_s, \Omega) = \mathcal{F}_t\{\mathcal{P}(\mathbf{x}_s, t)\}$ and $\hat{\mathcal{P}}(\mathbf{x}_{v'}, \Omega) = \mathcal{F}_t\{\mathcal{P}(\mathbf{x}_{v'}, t)\}$. Virtual illumination is usually defined in this time-frequency domain as a Gaussian pulse $\hat{\mathcal{P}}(\mathbf{x}_l, \Omega) \sim \mathcal{N}(\Omega_C, \sigma^2)$ and, in our case, simplified as a single virtual time-frequency $\hat{\mathcal{P}}(\mathbf{x}_l, \Omega) \sim \delta(\Omega_C)$. The virtual image corresponds to the virtual reconstructed wavefield $\hat{\mathcal{P}}(\mathbf{x}_{v'}, \Omega)$, which is computed by propagating each response wavefield $\hat{\mathcal{P}}(\mathbf{x}_s, \Omega)$ from all points $\mathbf{x}_s \in \mathcal{S}$ to $\mathbf{x}_{v'} \in \mathcal{V}'$ (Fig. 3(d)) using the RSD integral in Eq. (1) as

$$\begin{aligned}\hat{\mathcal{P}}(\mathbf{x}_{v'}, \Omega) &= \int_{\mathcal{S}} \hat{\mathcal{P}}(\mathbf{x}_s, \Omega) g_z(\mathbf{x}_{v'}, \mathbf{x}_s, \Omega) d\mathbf{x}_s \\ &= \int_{\mathcal{S}} \hat{\mathcal{P}}(\mathbf{x}_s, \Omega) \frac{|\mathbf{x}_{v'} - \mathbf{x}_s|_z}{|\mathbf{x}_{v'} - \mathbf{x}_s|} \frac{e^{ik|\mathbf{x}_{v'} - \mathbf{x}_s|}}{|\mathbf{x}_{v'} - \mathbf{x}_s|} \frac{1}{i\lambda} d\mathbf{x}_s,\end{aligned}\quad (9)$$

where $|\mathbf{x}_{v'} - \mathbf{x}_s|$ is the distance between \mathbf{x}_s and $\mathbf{x}_{v'}$, $|\mathbf{x}_{v'} - \mathbf{x}_s|_z$ is the distance between \mathbf{x}_s and $\mathbf{x}_{v'}$ in the z direction, and $k = 2\pi\Omega/c$ is the wavenumber being c the speed of light. Figuratively, this process resembles using a virtual lens that focuses the response wavefield at different depths. Equation (9) is similar to Eq. (1) but operates on the virtual wavefield (the phasor field) rather than on the electromagnetic field.

Discrete virtual illumination and camera analogy. In practice, the impulse response function is measured at discrete points $[\mathbf{x}_l, \mathbf{x}_s]$ on the relay wall, and can be expressed as a linear equation system $\mathbf{h} = \mathbf{A}\mathbf{v}$, where $\mathbf{h} \equiv H[\mathbf{x}_l, \mathbf{x}_s, t]$ is the discretized impulse response function, \mathbf{v} is the hidden scene representation (e.g. hidden object albedo), and \mathbf{A} is the forward operator that models time-resolved light transport [13]. From the discrete impulse response function $H[\mathbf{x}_l, \mathbf{x}_s, t]$, the discrete virtual response wavefield $\mathbf{s} \equiv \mathcal{P}[\mathbf{x}_s, t]$ is computed by virtually illuminating the hidden scene with arbitrary illumination $\mathcal{P}[\mathbf{x}_l, t]$:

$$\mathbf{s} \equiv \mathcal{P}[\mathbf{x}_s, t] = \sum_{\mathbf{x}_l \in \mathcal{L}} \mathcal{P}[\mathbf{x}_l, t] * H[\mathbf{x}_l, \mathbf{x}_s, t], \quad (10)$$

which is the discrete version of Eq. (8). Transforming it to the time-frequency domain with the Fourier transform with respect to time yields $\mathbf{s}_\Omega \equiv \hat{\mathcal{P}}[\mathbf{x}_s, \Omega] = \mathcal{F}_t[\mathbf{s}]$. The virtual reconstructed wavefield is computed, in matrix-vector formulation similarly to Eq. (6), as

$$\hat{\mathbf{v}}_{pf} = \mathbf{g}_z \mathbf{s}_\Omega, \quad (11)$$

where $\hat{\mathbf{v}}_{pf} \equiv \hat{\mathcal{P}}[\mathbf{x}_{v'}, \Omega]$ is the discrete reconstructed wavefield and \mathbf{g}_z the forward diffraction operator based on the RSD. Note that Eq. (11) is the discrete version of Eq. (9), and it solves the inverse problem of the hidden scene reconstruction with the forward diffraction operator \mathbf{g}_z , which seems counterintuitive.

3.3. Inverse diffraction

Forward diffraction computes the output wavefield $u_z(x, y)$ by propagating the input field $u_0(x, y)$ with the forward wave diffraction operator $g_z(x, y)$ as described by Eq. (1). Phasor Fields reconstructs the hidden scene in NLOS imaging using the forward diffraction operator $g_z(x, y)$, as described by Eq. (9). In contrast, inverse diffraction attempts to recover the input field $u_0(x, y)$ defined at object plane $z = 0$ given the observation of the output field $u_z(x, y)$ defined at the sensor plane $z > 0$. Analytical expressions for inverse diffraction have been studied [21,22], although the forward diffraction kernel $g_z(x, y)$ is singular due to evanescent waves [21,33,34]. We can analyze inverse diffraction in spatial-frequency domain where, assuming infinite and continuous

length planes, the exact inverse of the forward diffraction kernel $G_z^{-1}(f_x, f_y)$ can be decomposed into two terms [34] as

$$G_z^{-1}(f_x, f_y) = G_z^*(f_x, f_y) + K_z(f_x, f_y), \quad (12)$$

where $G_z^*(f_x, f_y)$ is the complex conjugate, defined as

$$G_z^*(f_x, f_y) = (e^{ikzm})^* = (e^{-ikzm^*}), \quad (13)$$

and it is an approximation of inverse diffraction with decaying exponential evanescent waves. $K_z(f_x, f_y)$ accounts for the effect of the inversion of the evanescent waves that, if discarded due to their exponential decay (Section 3.1), then the inverse becomes $G_z^{-1}(f_x, f_y) = G_z^*(f_x, f_y)$ and $g_z^{-1}(x, y) = g_z^\dagger(x, y)$, where the \dagger symbol denotes the adjoint (conjugate transpose) operator, and the forward diffraction operator becomes unitary [23]. As a consequence, inverse diffraction amounts to backward (negative distance) propagation $G_z^{-1}(f_x, f_y) = G_z^*(f_x, f_y) = G_{-z}(f_x, f_y)$ and $g_z^{-1}(x, y) = g_z^\dagger(x, y) = g_{-z}(x, y)$ [23,24,34,35]. Additionally, inverse diffraction can be performed with the forward diffraction operator in a formulation known as the *reciprocity theorem* [22], defined as

$$\hat{u}_0(x, y) = (g_z(x, y) * u_z^*(x, y))^* \quad (14)$$

and

$$\hat{U}_0(f_x, f_y) = (G_z(f_x, f_y) \cdot U_z^*(f_x, f_y))^*. \quad (15)$$

It consists on phase-conjugating the output wavefield, forward propagating and phase-conjugating the resulting field. The *reciprocity theorem* allows us to explain how a forward propagation operator can be used for solving an inverse problem, as in Phasor Fields (Section 4.1).

Inverse diffraction with finite discrete apertures. Inverse diffraction is an ill-posed problem for discretely sampled and finite apertures due to the singularity of the discrete forward diffraction operators \mathbf{g}_z and \mathbf{G}_z (Section 3.1), even if only homogeneous waves are considered. Conceptually, in discrete forward diffraction not all information from the original wavefield is preserved in the output wavefield, as it is only sampled at a finite number of discrete points. Consequently, completely reversing the process of forward diffraction to perfectly restore the input wavefield is not possible [35].

Due to the singularity of the discrete forward diffraction operator, the options for computing discrete inverse diffraction kernels are using either the matrix pseudoinverse $\tilde{\mathbf{g}}_z^{-1}$ or the matrix adjoint (conjugate transpose) \mathbf{g}_z^\dagger , but they are not equal ($\tilde{\mathbf{g}}_z^{-1} \neq \mathbf{g}_z^\dagger$) since the unitary property is lost in the discrete version of the forward diffraction operator. The pseudoinverse diffraction operator is numerically unstable due to the singularity of the discretized forward diffraction operator, needing numerical regularization techniques like Truncated Singular Value Decomposition (TSVD) to improve its stability. In spatial-frequency domain, the inverse diffraction form is defined as the element-wise reciprocal matrix $\tilde{\mathbf{G}}_z^{-1} = 1/\mathbf{G}_z$, which suffers also numerical instability when spatial-frequency values approach zero. A detailed discussion on sampling requirements and quality of inverse diffraction is presented by Katovnik *et al.* [35]. The stability difference between adjoint and inverse operators is known in other fields like geophysics [36].

To recapitulate, discrete inverse diffraction, being an ill-posed problem, can be performed in several ways, which are summarized in Eqs. (18) to (23) contained in Table 1:

- Numerically approximating the inverse, as described by Eqs. (18) and (19).
- Using Eq. (12), discarding evanescent waves (K_z) and therefore approximating the inverse with the adjoint, as described by Eqs. (20) and (21).
- Applying the *reciprocity theorem*, shown in Eq. (14), and using the forward diffraction operator, as illustrated by Eqs. (22) and (23).

Table 1. Forward diffraction (presented in Section 3.1 and here in Eq. (16) and Eq. (17)) and inverse diffraction in space domain and in spatial-frequency domain. Inverse diffraction can be performed by: numerically approximating the inverse operator (pseudoinverse matrix in Eq. (18) and reciprocal matrix in Eq. (19)), using the adjoint operator (Eq. (20) and Eq. (21)) and with the *reciprocity theorem* (Eq. (22) and Eq. (23)). In forward diffraction, the direction of propagation and the wavefield form is the same. Inverse diffraction can be performed by keeping the wavefield form and reversing the direction of propagation (inverse and adjoint forms) or reversing the wavefield by phase conjugation (reversing the wavefield form) and keeping the direction of propagation, using the forward propagator (*reciprocity theorem* form).

	Spatial domain	Spatial-frequency domain	Illustrative Diagram
Forward	$\mathbf{u}_z = \mathbf{g}_z \mathbf{u}_0$ (16)	$\mathbf{U}_z = \mathbf{G}_z \cdot \mathbf{U}_0$ (17)	
Pseudoinverse	$\hat{\mathbf{u}}_0 = \tilde{\mathbf{g}}_z^{-1} \mathbf{u}_z$ (18)	$\hat{\mathbf{U}}_0 = \tilde{\mathbf{G}}_z^{-1} \cdot \mathbf{U}_z$ (19)	
Adjoint	$\hat{\mathbf{u}}_0 = \mathbf{g}_z^\dagger \mathbf{u}_z$ (20)	$\hat{\mathbf{U}}_0 = \mathbf{G}_z^* \cdot \mathbf{U}_z$ (21)	
Reciprocity Theorem	$\hat{\mathbf{u}}_0 = (\mathbf{g}_z \mathbf{u}_z^*)^*$ (22)	$\hat{\mathbf{U}}_0 = (\mathbf{G}_z \cdot \mathbf{U}_z^*)^*$ (23)	

All three cases can be described in both space and spatial-frequency domain.

Physical interpretation of inverse diffraction. Inverse and adjoint diffraction methods are computational approaches for backward propagation, differing in their handling of evanescent waves [34]. The adjoint method approximates the inverse but fails to fully recover evanescent waves, while the inverse method amplifies their exponential decay. Since an analytical inverse of the diffraction operator does not exist, we revert to compute a pseudoinverse operator. Nonetheless, inverse diffraction based on computational backward propagation methods is valuable in fields like digital and computer generated holography [24]. However, inverse diffraction described by the *reciprocity theorem* is physically feasible using optical phase conjugation (OPC) elements, like a conjugate mirror or a forward phase conjugator [37].

Dual space. Diffraction exhibits symmetry due to its unitary property. While wavefields physically consist of positive frequencies propagated by the forward diffraction operator, using complex numbers opens the possibility of having negative frequencies (conjugates of the positive frequencies) that are propagated by the adjoint operator, forming a dual space [23,38]. In the

primary space, forward diffraction propagates positive frequencies forward, while the adjoint propagates them backward. In the dual space, the roles reverse: the forward diffraction operator produces backward propagation and the adjoint diffraction operator produces forward propagation of the negative frequency wavefield. These symmetries are bound to the sign used in the diffraction kernel, and linked through the reciprocity theorem and wavefield conjugation.

The physical meaning of inverse diffraction forms and the dual space formulation are used in Section 4.1 to give different physical interpretations to the role of the relay wall in Phasor Fields, and propose the new reconstruction method.

4. Inverse phasor fields

Phasor Fields transforms the NLOS problem into a virtual LOS problem, and reconstructs the hidden object using a (forward) diffraction operator for the virtual wavefields (Section 3.2). In contrast, other NLOS methods use inverse operators, like backprojection that uses the adjoint time-resolved light transport operator (Section 2). Forward and inverse models in NLOS imaging resemble forward (Section 3.1) and inverse diffraction (Section 3.3) models. In this section, we use the relationship between forward and inverse diffraction to explore why Phasor Fields can use a forward diffraction operator to reconstruct the hidden object (Section 4.1) and propose a new reconstruction method named Inverse Phasor Fields (Section 4.2).

4.1. Forward and backward propagation in phasor fields

Diffraction and NLOS imaging are very similar. Both have an object which defines the input value (input wavefield at the object plane \mathbf{u}_0 in diffraction and albedo values of the object \mathbf{v} in NLOS) and a measurement of the input at some plane (output wavefield at the sensor plane \mathbf{u}_z in diffraction and the impulse response function \mathbf{h} at the relay wall). The forward model describes the measured outputs given the inputs (forward diffraction \mathbf{g}_z and forward time-resolved light transport model \mathbf{A} in NLOS) and the inverse problem consists on estimating the input values given the measured outputs. The inverse problem in NLOS is modeled differently depending on the reconstruction method used.

Of particular interest is the Phasor Fields framework (Section 3.2), which transforms the impulse response function \mathbf{h} into a virtual response wavefield \mathbf{s} by virtually illuminating the hidden scene. Then, it converts the virtual response wavefield to time-frequency domain \mathbf{s}_Ω and propagates it using the forward diffraction propagator \mathbf{g}_z to imagine the hidden object $\hat{\mathbf{v}}_{pf}$. The use of a forward diffraction propagator \mathbf{g}_z , based on the RSD, to solve the inverse problem, which seems counterintuitive, is explained by making the analogy between the relay wall and a virtual lens. This analogy is useful for bringing tools from optics to Phasor Fields, and in consequence to NLOS. For instance, Luesia *et al.* introduce virtual zone plates for a lower-memory usage when propagating the virtual wavefield [39].

Still, this virtual lens analogy does not fully clarify why it is possible to solve an inverse problem using a forward propagator. We tackle this from the diffraction theory given in Section 3.1 and Section 3.3: we propose two complementary analogies of Phasor Fields, additionally to the lens analogy, that give different physical interpretation to the relay wall and the process of image formation as an inverse diffraction process. They are derived as direct identification with the inverse diffraction forms (Table 1) and the dual space formulation:

- **Relay wall as (forward) phase conjugator:** This interpretation assumes that the diffraction operator is correctly expressed as the forward diffraction operator in Eq. (11). Then, the virtual response wavefield at the relay wall must be equivalent to the conjugated output wavefield $\mathbf{s}_\Omega \equiv \mathbf{u}_z^*$, and applying the forward wave diffraction operator \mathbf{g}_z allows to estimate the hidden object, which would be equivalent to the restored conjugated input wavefield $\hat{\mathbf{v}}_{pf} \equiv \hat{\mathbf{u}}_0^*$. In practice, we only care about the amplitude of the reconstructed virtual

wavefield, so the conjugation difference can be disregarded. The equivalence between the virtual response wavefield and the conjugated output wavefield suggest that we can interpret that the relay wall is working as a phase conjugator and, in consequence, allows us to explain Phasor Fields as inverse diffraction using the *reciprocity theorem* in the virtual domain. This analogy effectively explains the use of a forward operator for solving an inverse problem.

- **Relay wall as hologram recorder:** This interpretation assumes that the virtual response wavefield at the relay wall is equivalent to the output wavefield $\mathbf{s}_\Omega \equiv \mathbf{u}_z$. As a consequence, the diffraction operator (with correct physical meaning) should be the adjoint \mathbf{g}_z^\dagger , which performs backward propagation to estimate the hidden object and has the same form as the forward diffraction operator but changing the direction of propagation, a change of sign in the diffraction kernel of Eq. (2). This is due to the unitary property of the diffraction operator. The hidden object estimation would be equivalent to the restored input wavefield $\hat{\mathbf{v}}_{pf} \equiv \hat{\mathbf{u}}_0$. In this analogy, the relay wall is acting as hologram recorder, the virtual response wavefield is an hologram and the reconstruction of the hidden object is performed by backpropagation of the virtual response wavefield, similarly to simulated reconstruction of digital holograms [24]. Previous works on Phasor Fields hint this analogy [40,41] and other NLOS reconstruction methods already used holographic techniques [42].

These interpretations are not exclusive due to the dual nature of forward and inverse diffraction operators. Each analogy can be understood as living in the dual space of the other. This means that the same numerical diffraction operator that is considered to be forward in the primary space with the phase conjugator analogy can be considered to be the adjoint operator in the dual space with the hologram recorder analogy. This is the reason why a forward diffraction operator can be used to solve an inverse problem: the *reciprocity theorem* describes how a forward operator in one space is equivalent to the adjoint (inverse) operator in its dual space. This duality of which diffraction operator, forward or backward, is being used is already present in previous works on Phasor Fields, where some of them describe the RSD integral with a $+i$ sign in the exponent [8,43] and others use a $-i$ sign in the exponent [9,39] when presenting the wave diffraction propagator. The reason is that Phasor Fields works on a virtual world where forward and backward operators are just a matter of convention depending on the sign of the Fourier transform used to define the virtual response wavefield in time-frequency domain.

4.2. Our approach: inverse phasor fields

The analogy of the relay wall as a virtual camera intuitively explains how Phasor Fields reconstructs the hidden object (Section 3.2). We have proposed two new analogies of Phasor Fields (Section 4.1) that explain it as inverse diffraction methods for solving the hidden object reconstruction, even though initially it might appear using a forward (diffraction) operator. The relay wall as phase conjugator analogy can be interpreted as inverse diffraction by the *reciprocity theorem* principle, using the forward diffraction operator on the conjugated wavefield. The relay wall as hologram recorder analogy explains how the hidden scene reconstruction is done by using the adjoint diffraction operator simulating backward propagation. These relay wall analogies represent two of the three inverse diffraction forms described in Table 1. In this section, we explore the missing inverse diffraction form described by Eqs. (18) and (19): we simulate backward propagation by numerically approximating the inverse in a method that we name Inverse Phasor Fields, because it actually inverts the propagation.

To achieve this, we propose to pose the hidden object reconstruction as an inverse diffraction problem, following previous methods in holography [25]. We define the image formation model

in the virtual world (time-frequency domain) as

$$\mathbf{s}_\Omega = \mathbf{g}_z \mathbf{v}_{vw}, \quad (24)$$

which describes the formation of the virtual response wavefield \mathbf{s}_Ω at the relay wall given the hidden scene representation in the virtual world \mathbf{v}_{vw} and the forward diffraction operator \mathbf{g}_z . This image formation resembles the light transport described by phasor imaging for continuous temporally modulated light [44], since the phasor field is a virtual modulation of light at MHz-range frequencies equivalent to virtual phasor imaging [40,43]. This formulation is similar to the forward diffraction model in Eq. (16), and the image formation model in NLOS (Section 3.2), but defined in time-frequency domain instead of the time domain (i.e. $\mathbf{h} = \mathbf{A}\mathbf{v}$). Also note that the virtual response wavefield \mathbf{s}_Ω can be acquired directly with the Fourier Domain Histogram technique [9] and not only as a postprocess on the impulse response signal.

From the virtual world image formation model in Eq. (24), we want to reconstruct an estimation of the hidden scene $\hat{\mathbf{v}}_{vw}$ given the known virtual response wavefield in time-frequency domain \mathbf{s}_Ω . Because this formation model in the virtual world is described by virtual forward diffraction, we can use the inverse diffraction forms (Table 1) as

$$\hat{\mathbf{v}}_{vw} = \tilde{\mathbf{g}}_z^{-1} \mathbf{s}_\Omega \quad (25a)$$

$$\hat{\mathbf{v}}_{vw} = \mathbf{g}_z^\dagger \mathbf{s}_\Omega \quad (25b)$$

$$\hat{\mathbf{v}}_{vw} = (\mathbf{g}_z \mathbf{s}_\Omega^*)^*. \quad (25c)$$

The reconstruction in Eq. (25a) uses the pseudoinverse operator $\tilde{\mathbf{g}}_z^{-1}$, since the forward diffraction operator \mathbf{g}_z is not invertible (Section 3.3). The pseudoinverse operator computes the hidden scene representation $\hat{\mathbf{v}}_{vw}$ that solves the linear least squares problem [45, Chapter 6],

$$\hat{\mathbf{v}}_{vw} = \tilde{\mathbf{g}}_z^{-1} \mathbf{s}_\Omega = \arg \min_{\mathbf{v}_{vw}} \|\mathbf{g}_z \mathbf{v}_{vw} - \mathbf{s}_\Omega\|^2. \quad (26)$$

However, this approach might be ill-conditioned, as small perturbations in the virtual response wavefield \mathbf{s}_Ω or the pseudoinverse diffraction operator $\tilde{\mathbf{g}}_z^{-1}$ may cause large perturbations of the solution $\hat{\mathbf{v}}_{vw}$. Regularization techniques, which we discuss later, address this issue. On the other hand, reconstructions given by Eq. (25b) and Eq. (25c) correspond to inverse diffraction forms based on the adjoint diffraction operator (hologram recorder analogy) and the *reciprocity theorem* (phase conjugator analogy). Note how these equations are similar to the initial camera analogy explanation in Eq. (11), but swapping the forward and the adjoint operators in Eq. (25b) and with a conjugation difference in Eq. (25c). These differences are explained in Section 4.1 as a duality in operators based on a convention that depends on the sign of the Fourier transform. For this reason, the reconstructions based on these methods are similar between them and with respect to Phasor Fields, because they are dual and equivalent approaches (Section 4.1).

We evaluate our reconstruction methods (Eqs. (25a) to (25c)) on two real scenes, *letter4* and *NLOSletter*, from publicly available data provided in Liu *et al.* work [9] (Liu dataset). The capture setup consists of a gated single-photon avalanche diode (SPAD) and a pico-second laser. The geometry is at distance $D = 0.75m$ in *letter4* and $D = 1.00m$ in *NLOSletter*. The system's temporal resolution is 70ps, and the relay wall has dimensions of 1.8m by 1.3m with a point spacing $\Delta \mathbf{x}_s = 0.01m$, yielding a 181×131 spatial grid of time measurements $H(\mathbf{x}_t, \mathbf{x}_s, t)$ for each scene. We refer to the original paper [9] for the full details of the acquisition setup.

Figure 4 shows the reconstruction of *letter4* and *NLOSletter* scenes with our approaches based on inverse diffraction. We virtually illuminate the hidden scene, with a single virtual wavelength $\lambda_v = 6 \Delta \mathbf{x}_s = 0.06m$, to compute the virtual wavefield \mathbf{s}_Ω at the relay wall. Then, we apply Eqs. (25a) to (25c) to obtain the reconstruction of the hidden scene $\hat{\mathbf{v}}_{vw}$. In all approaches, the reconstruction is correct where the hidden geometry is present but the artifacts in the empty

space are different between the pseudoinverse approach and the others. This is due to the fact that the solution given by the adjoint and the reciprocity theorem are mathematically equivalent (which is the solution by standard Phasor Fields). Then, when comparing with the pseudoinverse, the source of the artifacts where no geometry is present is fundamentally different: in the case of standard Phasor Fields the errors come from the resolution limits at specific frequencies, while the errors on the numerical pseudoinverse come from the ambiguities and ill-posedness of the propagation matrix. While both types solutions seem to be equivalent in terms of error, the adjoint and reciprocity theorem versions are more robust operators [36].

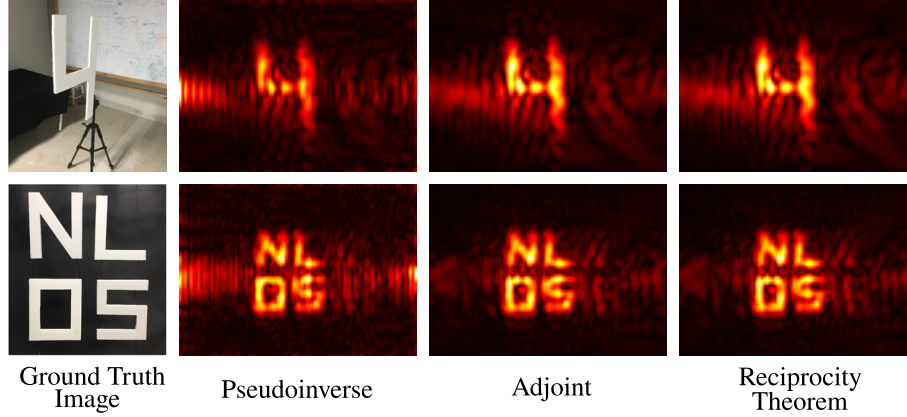


Fig. 4. Hidden object reconstructions of (up) *letter4* and (bottom) *NLOSletter* scenes, from *Liu* dataset [9], with our three inverse diffraction forms: pseudoinverse matrix (Eq. (25a)), adjoint matrix (Eq. (25b)) and *reciprocity theorem* (Eq. (25c)). Scenes have been virtually illuminated with a single virtual wavelength $\lambda_v = 0.06m$. We show the amplitude of the reconstructed wavefield $|\hat{\mathbf{v}}_{vw}|$ at the hidden object depth $z = D$, with $D = 0.75m$ in *letter4* scene and $D = 1.00m$ in *NLOSletter* scene. The geometry reconstructions are similar for all of our methods but the surrounding artifacts vary between the pseudoinverse approach and the others.

Filtering. Most NLOS reconstruction algorithms apply filters to separate the signal from the noise in the measurements. In backprojection, the Laplacian filter is used, while in Phasor Fields this filtering comes from the virtual frequencies chosen when performing the virtual illumination of the scene. In our Inverse Phasor Fields method, filtering comes from the numerical algorithm used to compute the pseudoinverse diffraction operator $\tilde{\mathbf{g}}_z^{-1}$. We use the Singular Value Decomposition (SVD) method that decomposes the forward diffraction operator in a set of orthonormal bases $\mathbf{a}_1, \dots, \mathbf{a}_m$ and $\mathbf{b}_1, \dots, \mathbf{b}_n$, called left singular vectors and right singular vectors, and singular values σ_i as

$$\mathbf{g}_z = \sum_{i=1}^r \mathbf{a}_i \sigma_i (\mathbf{b}_i^*)^T \quad (27)$$

where $r = \min(m, n)$ is the rank of $\tilde{\mathbf{g}}_z^{-1}$ and the singular values are sorted in non-increasing order. The pseudoinverse operator $\tilde{\mathbf{g}}_z^{-1}$ is computed as

$$\tilde{\mathbf{g}}_z^{-1} = \sum_{i=1}^r \mathbf{b}_i \frac{1}{\sigma_i} (\mathbf{a}_i^*)^T. \quad (28)$$

Given the ill-conditioned nature of our problem, we regularize the solution with Truncated Singular Value Decomposition (TSVD) where we truncate the summation in Eq. (28) at a value

$t < r$ such that all the small singular values are discarded. We define a more intuitive parameter $t_{th} \in [0, 1]$ which discards all the singular values $\sigma_i \leq t_{th} \sigma_{max}$, where σ_{max} is the maximum singular value. Existing research shows that results from Tikhonov regularization and TSVD are similar [46,47].

We compare reconstructions of *letter4* and *NLOSletter* scenes with pseudoinverse operators computed with different thresholds t_{th} , shown in Fig. 5. After applying a virtual illumination in time-frequency domain $\hat{\mathcal{P}}(\mathbf{x}_l, \Omega)$ with single virtual wavelength $\lambda_v = 6 \Delta \mathbf{x}_s = 0.06m$, we reconstruct the hidden scene with the truncated pseudoinverse operator $\hat{\mathbf{g}}_z^{-1}(t_{th})$, where the parenthesis makes explicit the different pseudoinverse operators depending on the threshold parameter. When the threshold is very low (no singular value is discarded), the regularization's effect is very low and the geometry is not reconstructed because the noise in the measurements and the ill-posedness of the problem is predominant. When the threshold is increased, the geometry is increasingly better reconstructed, because the reconstruction technique avoids overfitting to the noise in the measurements. If the threshold is set too high, too many singular values are discarded, leading to an incorrect reconstruction due to the significant loss of information during the regularization. The appropriate threshold parameter depends on the scene setup, although a value in the range $t_{th} \in [0.1, 0.2]$ is a reasonable estimate that discards small singular values while preventing an overly low-rank approximation of the pseudoinverse operator.

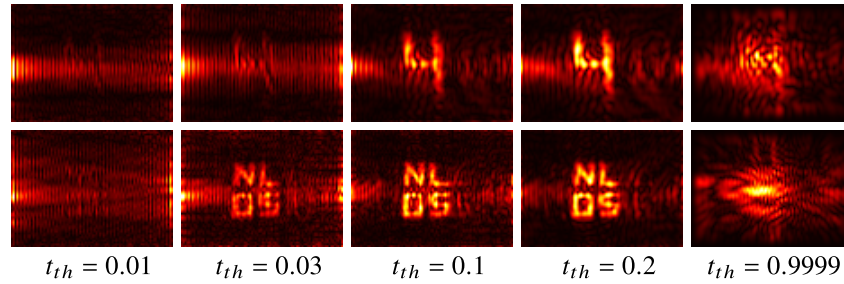


Fig. 5. Comparison of hidden object reconstructions of (up) *letter4* and (bottom) *NLOSletter* scenes, from *Liu* dataset [9], with our method based on the pseudoinverse diffraction operator $\hat{\mathbf{g}}_z(t_{th})$ and different TSVD thresholds t_{th} . Scenes have been virtually illuminated with a single virtual wavelength $\lambda_v = 0.06m$. We show the amplitude of the reconstructed wavefield $|\hat{\mathbf{v}}_{vw}|$ at the hidden object depth $z = D$, with $D = 0.75m$ in *letter4* scene and $D = 1.00m$ in *NLOSletter* scene. When a low threshold t_{th} is used (few singular values discarded), the geometry is not reconstructed due to the problem's ill-posed nature. Increasing the threshold improves reconstruction by reducing noise overfitting. However, setting the threshold too high discards too much information, resulting in incorrect reconstruction.

Multiple wavelengths. In Phasor Fields formulation, the virtual illumination pulse is usually defined as a Gaussian pulse in time-frequency domain (Section 3.2). Then, the virtual response wavefield is propagated by the RSD to compute the reconstructed wavefield for each individual virtual wavelength. The final reconstruction is expressed as a superposition of the reconstructed wavefield for each virtual wavelength. In single wavelength reconstructions, the wavefield at depths z different from the depth D where the hidden object is appear as unfocused wavefields (third and fifth row in Fig. 6(a) and Fig. 6(b)) but, in comparison, using multiple frequencies allows to reconstruct the object only at the correct depth (fourth and sixth row in Fig. 6(a) and Fig. 6(b)). The intuition is that using multiple virtual wavelengths creates destructive interferences at incorrect depths and constructive interferences at the correct depth, revealing the hidden geometry. Our Inverse Phasor Fields approach also supports multiwavelength reconstructions (second row in Fig. 6(a) and Fig. 6(b)), by solving the inverse diffraction problem for each

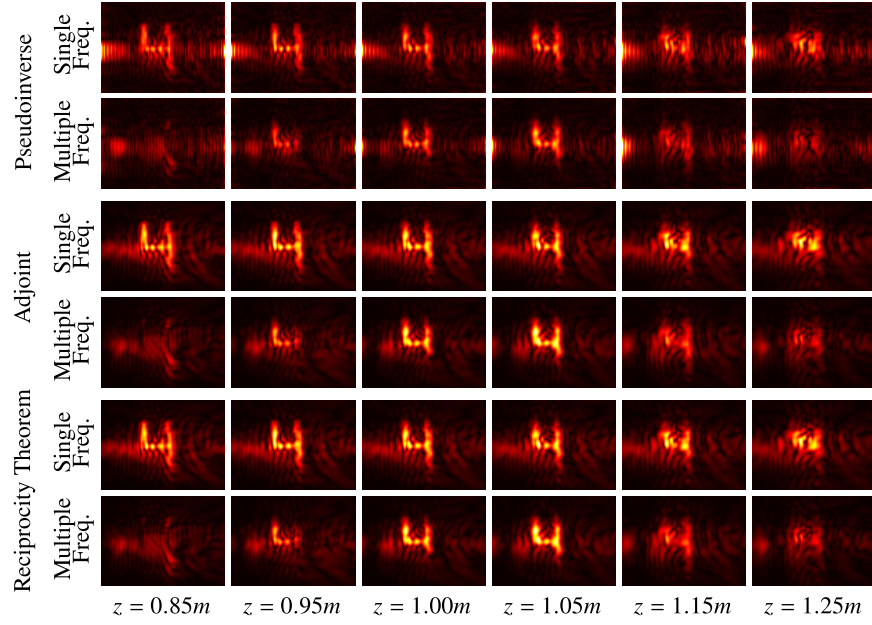
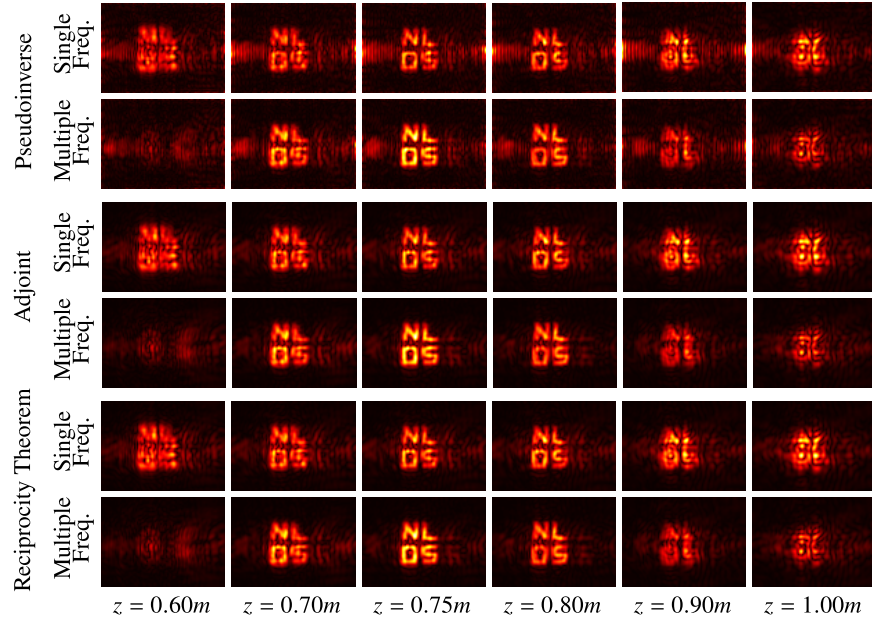
(a) Reconstructions of scene *letter4*. Hidden object is at depth $D = 1.00m$.(b) Reconstructions of scene *NLOSletter*. Hidden object is at depth $D = 0.75m$.

Fig. 6. Comparison between single and multiple wavelength reconstructions of (a) *letter4* and (b) *NLOSletter* scenes, from *Liu* dataset [9], with our inverse diffraction forms (pseudoinverse, adjoint and reciprocity theorem) at different depths z . Single wavelength reconstructions ($\lambda_v = 0.06m$) show signal even at depths z different from the hidden geometry depth D while multi wavelength reconstructions (mean virtual wavelength $\mu_v = 0.06$ and pulse width $\sigma_v = 0.1$) show signal mostly at depths z close to the hidden geometry depth D .

individual virtual wavelength and superimposing them latter in a similar manner to the Phasor Fields method.

5. Computational metric for NLOS reconstruction limits

NLOS imaging, as any imaging system, presents limits when reconstructing the hidden scene depending on the capture setup, resolution on the relay wall and reconstruction method. In the case of our proposed Inverse Phasor Fields, these limits can be understood as ambiguities in the formation of the signal at the relay wall from the hidden scene. This is the reason why the problem is ill-posed.

As propagation on the virtual world is modeled by forward diffraction matrix \mathbf{g}_z , this ill-posedness can be measured from the conditioning of the matrix. In particular, the rank of the matrix is related to this conditioning, so we define a computational metric r based on this rank, as

$$r = \frac{\text{rank}(\mathbf{g}_z)}{\text{rows}(\mathbf{g}_z)}, \quad (29)$$

which can take values from zero to one. The intuition behind the metric is that when it is close to one, $r \approx 1$, the matrix representation of the forward wave diffraction operator has full (or almost full) rank. In consequence, the specific NLOS setup is well-posed for reconstruction, which will have high detail because the reconstruction will have less ambiguities. If the metric is close to zero, $r \approx 0$, the NLOS setup to reconstruct the hidden scene is ill-posed, with the matrix having low rank, and the reconstruction will have lower detail because there will be more ambiguities. This metric is applicable to any NLOS setup regardless of the reconstruction method. In the context of our Inverse Phasor Fields approach (Section 4.2), which reconstructs the hidden scene by posing the NLOS imaging problem as an inverse diffraction problem, the metric directly describes how under-determined the diffractive linear system will be and the quality of the reconstruction. Related, but not equal, estimators exist in LOS optics based on the degrees of freedom of the diffraction operators [33] and in diffraction for holography applications [35].

In NLOS, the Rayleigh criterion has been adapted to the Phasor Fields framework [8] by identifying: the focal length f to the distance between the hidden object and the relay wall D , the size of the aperture \mathcal{A} to the number of sensed points in the relay wall N_s and its separation $\Delta \mathbf{x}_s$ and the virtual wavelength used in the reconstruction λ_v . Thus, the Rayleigh resolution limit adapted to Phasor Fields is defined as

$$\Delta x \approx 1.22 \frac{\lambda_v f}{\mathcal{A}} \equiv 1.22 \frac{\lambda_v D}{N_s \Delta \mathbf{x}_s}. \quad (30)$$

All these parameters (D , \mathcal{A} and λ_v) are implicit in the forward diffraction operator \mathbf{g}_z when it is computed, so our computational criterion also accounts for them. Note that our computational metric does not aim to estimate the Rayleigh limit criterion. While the Rayleigh limit criterion ranges from zero to infinity, our quality metric is normalized to span from zero to one. Rather, we show that reconstructions of NLOS setups having similar quality will yield comparable values of our quality metric and, also, the Rayleigh limit criterion, despite the two metrics differing between them.

We analyze both our quality metric and Rayleigh's criterion for different NLOS setups by varying the parameters present in the Rayleigh criterion; the distance between the object and the relay wall D , the size of the relay wall \mathcal{A} and the virtual wavelength λ_v . The test hidden scene is composed by a single object, the letter R, and we use *mitransient* [48], a transient renderer optimized for NLOS imaging [49], to simulate the acquisition of the impulse response signal of each scene. The simulated system has a temporal resolution of 100ps, with $N_s = 128$ yielding a 128×128 spatial grid of measurements $H(\mathbf{x}_l, \mathbf{x}_s, t)$ and varying dimensions of the relay wall

\mathcal{A} . As the distance D between the hidden object and the relay wall increases, reconstructions loose quality and become blurrier because the relative distance between resolvable points in the hidden object becomes smaller. Reconstructions with bigger virtual wavelengths λ_v have lower detail, since the wavefield is not able to represent lower detail information. This loss of detail is expressed by our estimator, which has values closer to one when using shorter wavelengths or when the object is closer to the relay wall, and has values closer to zero when bigger wavelengths are used or the object is further (Fig. 7(a) and Fig. 8). The size of the relay wall also affects the quality of the reconstruction. A bigger relay wall captures more information, which translates to more detailed reconstructions and higher values of our estimator (Fig. 7(b) and Fig. 9). In general, our estimator will have lower values in a setup with more ambiguities, which can be because of a big virtual wavelength, small aperture size or higher distance between the object and the relay wall. Notice that for very small wavelengths, compared to the size of the scene, both Rayleigh's criterion and ours indicate high quality but the reconstructions become very noisy (reconstructions with virtual wavelength $\lambda_v = 0.01\text{m}$ in Fig. 8). That is because for low wavelengths we are below the limit indicated by the Shannon-Nyquist sampling theorem.

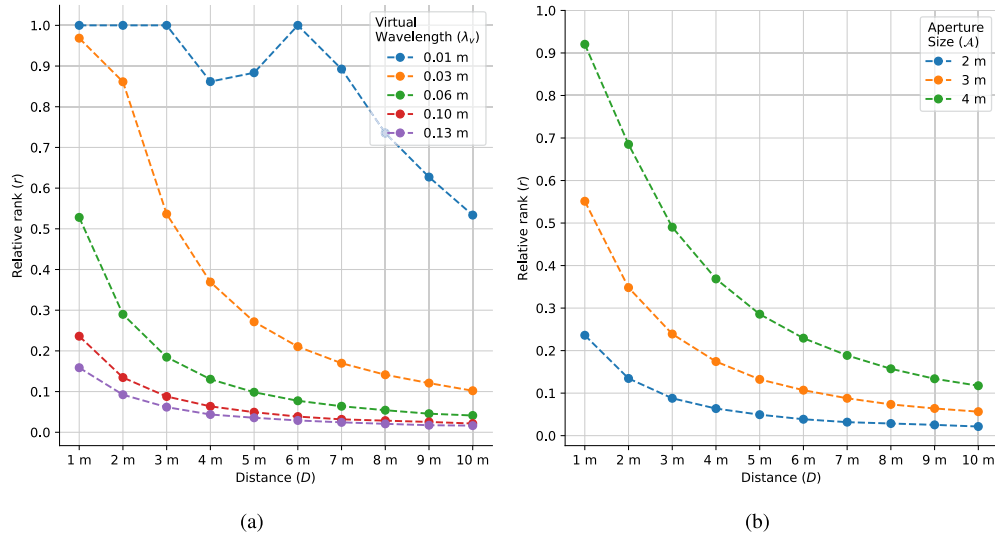


Fig. 7. Evolution of our computational metric r based on the relative rank of the forward diffraction operator \mathbf{g}_z at different distances D with (a) different virtual wavelengths λ_v and (b) different aperture sizes \mathcal{A} . Our computational metric has bigger values with smaller wavelengths or bigger aperture sizes because these NLOS setups present less ambiguities.

Resolution metrics, including our proposed metric and the Rayleigh resolution limit, typically define the maximum achievable resolution under ideal conditions, assuming full visibility of all objects from the relay wall. However, when occlusions occur, reconstruction quality degrades, even if objects are partially visible. This degradation arises because overlapping objects obstruct signal propagation, reducing the effective sensing area on the relay wall that receives signal from the overlapped objects. Since resolution metrics do not account for occlusions, they yield the same values for both occluded and non-occluded scenes, despite the former exhibiting lower detail (Fig. 10).

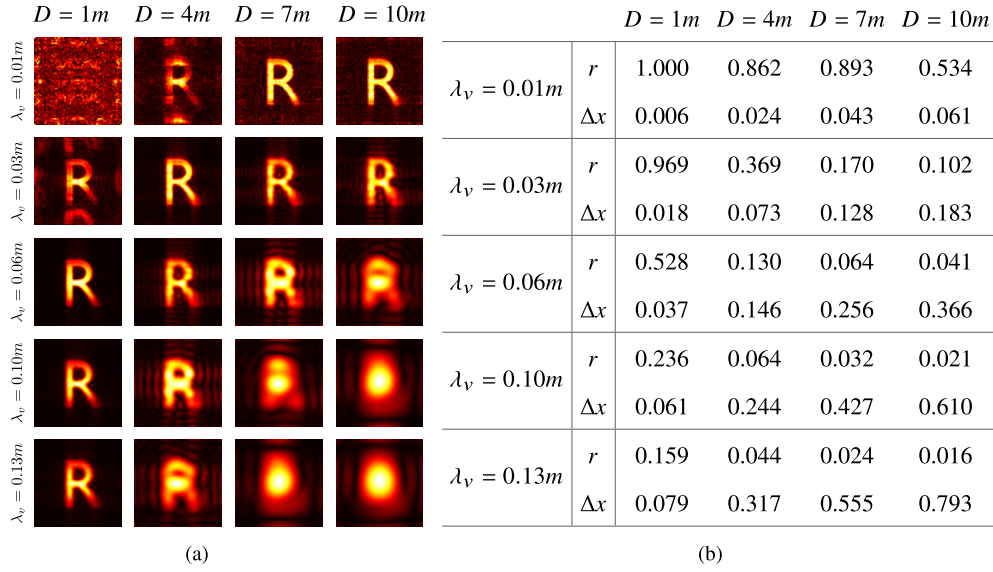


Fig. 8. (a) Reconstructions with geometry at different distances with different virtual wavelengths. (b) Our computational metric r and Rayleigh resolution limit Δx for the reconstructions. Reconstructions with similar quality, ($D = 4m, \lambda_v = 0.10m$) and ($D = 7m, \lambda_v = 0.06m$), have similar values for our computational metric and the Rayleigh resolution limit.

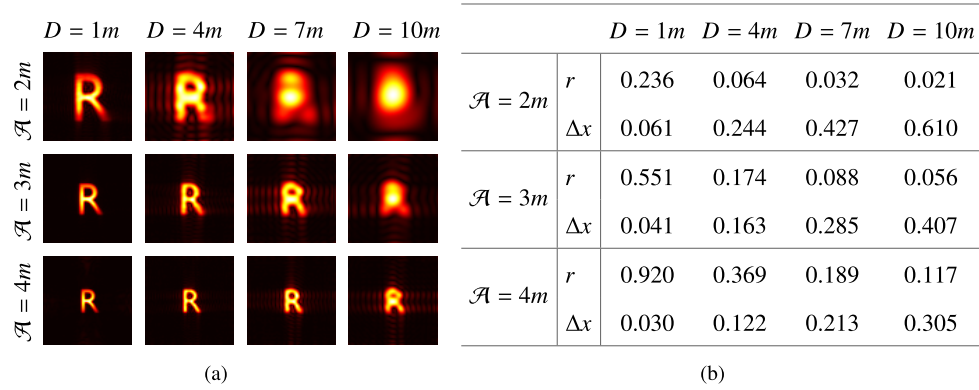


Fig. 9. (a) Reconstructions with geometry at different distances with different aperture sizes. (b) Our computational metric r and Rayleigh resolution limit Δx for the reconstructions. Reconstructions with bigger aperture sizes are smaller because of the relative size between the hidden object and the aperture (relay wall). Reconstructions with similar quality, ($D = 4m, \mathcal{A} = 2m$) and ($D = 7m, \mathcal{A} = 3m$), have similar values for our computational metric and the Rayleigh resolution limit.

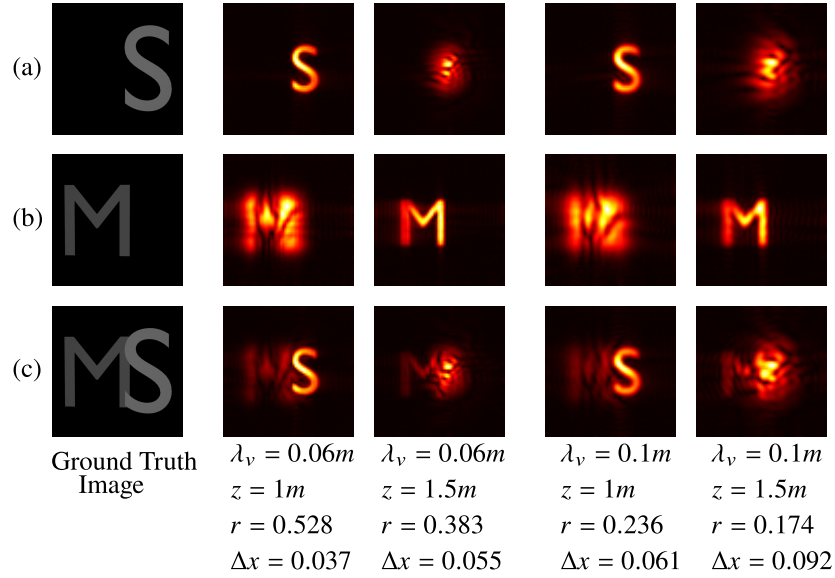


Fig. 10. Comparison of reconstructions with occlusions. The scenes contain objects at different depths: (a) letter S at $D_S = 1m$, (b) letter M at $D_M = 1.5m$ and (c) both letters at their respective depth. Reconstructions are performed using two virtual wavelengths ($\lambda_v = 0.06m$ in the second and third columns and $\lambda_v = 0.1m$ in the fourth and fifth columns) at two depths ($z = 1m$ in the second and fourth column and $z = 1.5m$ in the third and fifth columns). Our proposed quality metric r and the Rayleigh resolution limit Δx do not account for occlusions and assume full object visibility. As a result, the resolution metrics are the same for each combination of virtual wavelength and depth (each column) despite the degraded reconstruction of letter M in scene (c). Quality metrics compute the maximum resolution assuming the object is present at that depth. When reconstructing at depths $z \neq D_S, D_M$, out-of-focus artifacts appear, which can be addressed by multi-wavelength reconstructions.

6. Discussion and conclusion

In this work, we explore further the relationship between wave diffraction and NLOS imaging under the Phasor Fields framework, a method which presents the hidden scene reconstruction in NLOS imaging as a process of forward propagation of virtual waves using the RSD integral. Based on the inverse diffraction forms explored in optics, we explain how the counterintuitive use of the forward diffraction operator to solve the inverse problem of the hidden scene reconstruction can be interpreted as the application of the *reciprocity theorem* to NLOS imaging in the virtual domain introduced by Phasor Fields. This allows us to establish two additional analogies to the role of the relay wall, leveraging the physical meaning attributed to each type of inverse diffraction form: backwards propagation as a computational method to reconstruct a wavefield using the adjoint or pseudoinverse operator, as it is done in digital holography, or the application of the *reciprocity theorem* as a physical realizable method with phase conjugators. We translate these analogies to NLOS imaging, treating the relay wall as a forward phase conjugator or as an hologram recorder.

From these analogies, we propose Inverse Phasor Fields, a reconstruction method based on defining the image formation model of NLOS imaging in the virtual domain introduced by Phasor Fields, and performing the hidden scene reconstruction using inverse diffraction methods. The adjoint diffraction operator and the application of the *reciprocity theorem* yield equivalent results

to Phasor Fields, since they are dual and equivalent approaches, but the reconstructions with the pseudoinverse operator have its own particular trade-offs between reconstructed geometry and noise structure depending on the TSVD parameter. Phasor Fields, nevertheless, works due to the unitary property of continuous Rayleigh-Sommerfeld diffraction, because the adjoint propagator is reasonably similar to the inverse. Inverse Phasor Fields would generalize to scenarios in which the operator is not unitary anymore, such as in the case of relay surfaces of arbitrary geometry or reconstructions after several bounces of light, which we believe can inspire future research.

Additionally, based on the discrete representation of forward diffraction as matrix notation, we propose a computational quality metric for each concrete NLOS scene setup, that shows agreement with the well-known Rayleigh criterion for resolution used in optics and Phasor Fields. As noise is not part of the imaging setup but a sensor property, neither of both quality metrics accounts for it. Devising a quality metric that incorporates the effect of sensor noise is an interesting avenue for future work.

Insights gained from looking deeper into diffraction theory allow to understand better previous works in NLOS and Phasor Field-based works. For instance, Liu *et al.* [9] use a convolutional fast Fourier transform based RSD to reconstruct the hidden scene which is equivalent to the angular spectrum method, widely applied in diffraction theory. In addition, the missing cone problem, related to surface orientations not visible in NLOS reconstructions, is typically analyzed in spatial-frequency domain [11] and resembles the cone that partitions homogeneous and evanescent waves, suggesting a unified analysis of the missing cone incorporating homogeneous and evanescent waves in the virtual domain or using visualizations from diffraction theory, such as Ewald's sphere [24].

Usually, the backprojection algorithm is applied on filtered data or is followed by a filter to reduce light ambiguities when applying the adjoint of the time-resolved light transport operator, introducing a bias to the solution so that the reconstruction is cleaner. In our proposed method Inverse Phasor Fields, these filters that bias the solution become regularizations to compute the pseudoinverse diffraction operator using TSVD. In future works, different regularization terms (sparsity, L1 norm or total variation) could be added to a minimization framework in time-frequency space to bias the reconstructions, as it is done already in holography [25] or in NLOS imaging in time domain [5,17]. Moreover, existing literature in LOS optics and diffraction already relate backprojection methods and wave backpropagation methods [50,51].

The unitary property of the forward wave diffraction operator $g_z(x, y)$, if evanescent waves are discarded, introduces a dual space perspective where forward and backward diffraction operators have opposite meanings in the dual space. This dual perspective is also present in Phasor Fields, where the time-domain impulse response function is transformed into a time-frequency domain by using the Fourier transform. Since the Fourier transform can be defined with either the positive exponent $e^{i2\pi\Omega t}$ or the negative exponent $e^{-i2\pi\Omega t}$, the sign of the virtual frequencies of the virtual wavefield and the direction of the diffraction propagation operator is only a matter of convention that depend on the sign of the Fourier transform. This realization helps to explain why some Phasor Fields-based methods describe the RSD integral with a $+i$ sign in the exponent [8,43] (Fourier transform with the positive sign) and other use a $-i$ sign in the exponent [9,39] (Fourier transform with the negative sign) when applying wave diffraction propagation.

The unitary property of propagation operators has also been discussed in NLOS in a more general form using Dirac notation [52], in this case regarding point-to-point propagation. Dirac notation naturally accounts for the dual space perspective, that we have explored through the diffraction operator in this work.

In conclusion, this work presents a step towards a more unified view between the field of NLOS imaging and optics, especially between diffraction and Phasor Fields. We hope it can help bring existing tools from optics like super resolution, compressive sensing or extended depth of field to NLOS.

Funding. European Commission's HORIZON EUROPE Research and Innovation Actions (101070310); Ministerio de Ciencia, Innovación y Universidades (FPU23/03132).

Acknowledgment. The authors thank Pablo Luesia-Lahoz for proofreading the manuscript. This work has received funding from the European Commission's HORIZON EUROPE Research and Innovation Actions project Sestosenso under GA number 101070310. Jorge Garcia-Pueyo was supported by the FPU23/03132 predoctoral grant.

Disclosures. The authors declare no conflicts of interest.

Data availability. Code and data underlying the results presented in this paper are available in Ref. [53]. In addition, data corresponding to real NLOS scenes is available in the original paper [9].

References

1. A. Velten, T. Willwacher, O. Gupta, *et al.*, "Recovering three-dimensional shape around a corner using ultrafast time-of-flight imaging," *Nat. Commun.* **3**(1), 745 (2012).
2. V. Arellano, D. Gutierrez, and A. Jarabo, "Fast back-projection for non-line of sight reconstruction," *Opt. Express* **25**(10), 11574–11583 (2017).
3. B. Ahn, A. Dave, A. Veeraraghavan, *et al.*, "Convolutional approximations to the general non-line-of-sight imaging operator," in *IEEE/CVF International Conference on Computer Vision* (2019), pp. 7888–7898.
4. M. La Manna, F. Kine, E. Breibach, *et al.*, "Error backprojection algorithms for non-line-of-sight imaging," *IEEE Trans. Pattern Anal. Mach. Intell.* **41**(7), 1615–1626 (2019).
5. F. Heide, L. Xiao, W. Heidrich, *et al.*, "Diffuse mirrors: 3d reconstruction from diffuse indirect illumination using inexpensive time-of-flight sensors," in *Conference on Computer Vision and Pattern Recognition* (IEEE, 2014), pp. 3222–3229.
6. M. O'Toole, D. B. Lindell, and G. Wetzstein, "Confocal non-line-of-sight imaging based on the light-cone transform," *Nature* **555**(7696), 338–341 (2018).
7. D. B. Lindell, G. Wetzstein, and M. O'Toole, "Wave-based non-line-of-sight imaging using fast f-k migration," *ACM Trans. Graph.* **38**(4), 1–13 (2019).
8. X. Liu, I. Guillén, M. La Manna, *et al.*, "Non-line-of-sight imaging using phasor-field virtual waveoptics," *Nature* **572**(7771), 620–623 (2019).
9. X. Liu, S. Bauer, and A. Velten, "Phasor field diffraction based reconstruction for fast non-line-of-sight imaging systems," *Nat. Commun.* **11**(1), 1645 (2020).
10. J. W. Goodman, *Introduction to Fourier optics* (Roberts & Co., 2005).
11. X. Liu, S. Bauer, and A. Velten, "Analysis of feature visibility in non-line-of-sight measurements," in *IEEE/CVF Conference on Computer Vision and Pattern Recognition* (2019), pp. 10132–10140.
12. D. Royo, T. Sultan, A. Muñoz, *et al.*, "Virtual mirrors: Non-line-of-sight imaging beyond the third bounce," *ACM Trans. Graph.* **42**(4), 1–15 (2023).
13. D. Faccio, A. Velten, and G. Wetzstein, "Non-line-of-sight imaging," *Nat. Rev. Phys.* **2**(6), 318–327 (2020).
14. R. Geng, Y. Hu, Y. Chen, *et al.*, "Recent advances on non-line-of-sight imaging: Conventional physical models, deep learning, and new scenes," *APSIPA Trans. on Signal Inf. Process.* **11**(1), e1 (2022).
15. A. Jarabo, J. Marco, A. Muñoz, *et al.*, "A framework for transient rendering," *ACM Trans. Graph.* **33**(6), 1–10 (2014).
16. C.-Y. Tsai, A. C. Sankaranarayanan, and I. Gkioulekas, "Beyond volumetric albedo — a surface optimization framework for non-line-of-sight imaging," in *IEEE/CVF Conference on Computer Vision and Pattern Recognition* (2019), pp. 1545–1555.
17. F. Heide, M. O'Toole, K. Zang, *et al.*, "Non-line-of-sight imaging with partial occluders and surface normals," *ACM Trans. Graph.* **38**(3), 1–10 (2019).
18. D. Blinder, T. Birnbaum, T. Ito, *et al.*, "The state-of-the-art in computer generated holography for 3d display," *Light: Adv. Manufact.* **3**(3), 1 (2022).
19. A. C. Kak and M. Slaney, *Principles of Computerized Tomographic Imaging* (Society for Industrial and Applied Mathematics, 2001).
20. S. Mehrabkhani and T. Schneider, "Is the rayleigh-sommerfeld diffraction always an exact reference for high speed diffraction algorithms?" *Opt. Express* **25**(24), 30229–30240 (2017).
21. J. R. Shewell and E. Wolf, "Inverse diffraction and a new reciprocity theorem*," *J. Opt. Soc. Am.* **58**(12), 1596–1603 (1968).
22. E. Lalor, "A new approach to the inverse diffraction problem," *J. Phys. A: Gen. Phys.* **2**(2), 236–240 (1969).
23. W. D. Montgomery, "Basic duality in the algebraic formulation of electromagnetic diffraction," *J. Opt. Soc. Am.* **59**(7), 804–811 (1969).
24. K. Matsushima, *Introduction to computer holography*, Springer eBook Collection (Springer, 2020).
25. C. Fournier, L. Denis, E. Thiebaud, *et al.*, "Inverse problem approaches for digital hologram reconstruction," *Proc. SPIE - The Int. Soc. for Opt. Eng.* **8043**, 80430S (2011).
26. Y. Shechtman, Y. C. Eldar, O. Cohen, *et al.*, "Phase retrieval with application to optical imaging: A contemporary overview," *IEEE Signal Process. Mag.* **32**(3), 87–109 (2015).
27. T. Latychevskaia, J.-N. Longchamp, and H.-W. Fink, "When holography meets coherent diffraction imaging," *Opt. Express* **20**(27), 28871–28892 (2012).

28. M. Guizar-Sicairos, "Methods for coherent lensless imaging and x-ray wavefront measurement," Ph.D. thesis, University of Rochester (2010).
29. T. Latychevskaia, "Iterative phase retrieval for digital holography: tutorial," *J. Opt. Soc. Am. A* **36**(12), D31–D40 (2019).
30. T. Kreis, *Handbook of Holographic Interferometry* (John Wiley & Sons, Ltd, 2004).
31. H. N. Chapman and K. A. Nugent, "Coherent lensless x-ray imaging," *Nat. Photonics* **4**(12), 833–839 (2010).
32. L. Valzania, Y. Zhao, L. Rong, *et al.*, "Thz coherent lensless imaging," *Appl. Opt.* **58**(34), G256–G275 (2019).
33. F. G. M. Bertero, C. De Mol, and L. Ronchi, "Number of degrees of freedom in inverse diffraction," *Opt. Acta: Int. J. Opt.* **30**(8), 1051–1065 (1983).
34. J. Xiao, W. Zhang, and H. Zhang, "Inverse diffraction in phase space," *J. Opt. Soc. Am. A* **40**(1), 175–184 (2023).
35. V. Katkovnik, A. Migukin, and J. Astola, "Backward discrete wave field propagation modeling as an inverse problem: toward perfect reconstruction of wave field distributions," *Appl. Opt.* **48**(18), 3407–3423 (2009).
36. J. Claerbout, *Geophysical Image Estimation by Example* (Lulu.com, 2014).
37. G. S. He, "Optical phase conjugation: principles, techniques, and applications," *Prog. Quantum Electron.* **26**(3), 131–191 (2002).
38. A. W. Lohmann, J. Ojeda-Castaneda, and N. Streibl, "Symmetries in coherent and partially coherent fields," *Opt. Acta: Int. J. Opt.* **30**(4), 399–402 (1983).
39. P. Luesia-Lahoz, D. Gutierrez, and A. Muñoz, "Zone plate virtual lenses for memory-constrained nlos imaging," in *International Conference on Acoustics, Speech and Signal Processing* (IEEE, 2023), pp. 1–5.
40. S. A. Reza, M. L. Manna, S. Bauer, *et al.*, "Phasor field waves: A Huygens-like light transport model for non-line-of-sight imaging applications," *Opt. Express* **27**(20), 29380–29400 (2019).
41. C. Gu, T. Sultan, K. Masumnia-Bisheh, *et al.*, "Fast non-line-of-sight imaging with non-planar relay surfaces," in *International Conference on Computational Photography* (IEEE, 2023), pp. 1–12.
42. F. Willomitzer, P. V. Rangarajan, F. Li, *et al.*, "Fast non-line-of-sight imaging with high-resolution and wide field of view using synthetic wavelength holography," *Nat. Commun.* **12**(1), 6647 (2021).
43. S. A. Reza, M. L. Manna, S. Bauer, *et al.*, "Phasor field waves: experimental demonstrations of wave-like properties," *Opt. Express* **27**(22), 32587–32608 (2019).
44. M. Gupta, S. K. Nayar, M. B. Hullin, *et al.*, "Phasor imaging: A generalization of correlation-based time-of-flight imaging," *ACM Trans. Graph.* **34**(5), 1–18 (2015).
45. S. Axler, *Linear algebra done right*, Undergraduate texts in mathematics (Springer International Publishing, 2023), 4th ed.
46. P. C. Hansen, "The truncatedsvd as a method for regularization," *BIT* **27**(4), 534–553 (1987).
47. T. F. Chan and P. C. Hansen, "Computing truncated singular value decomposition least squares solutions by rank revealing qr-factorizations," *SIAM J. Sci. and Stat. Comput.* **11**(3), 519–530 (1990).
48. D. Royo, M. Crespo, and J. Garcia-Pueyo, "mitransient," <https://github.com/diegoroyo/mitransient> (2023).
49. D. Royo, J. García, A. Muñoz, *et al.*, "Non-line-of-sight transient rendering," *Comput. & Graph.* **107**, 84–92 (2022).
50. C. Esmersoy and D. Miller, "Backprojection versus backpropagation in multidimensional linearized inversion," *Geophysics* **54**(7), 921–926 (1989).
51. T. C. Wedberg, J. J. Stamnes, and W. Singer, "Comparison of the filtered backpropagation and the filtered backprojection algorithms for quantitative tomography," *Appl. Opt.* **34**(28), 6575–6581 (1995).
52. A. Redo-Sanchez, P. Luesia-Lahoz, D. Gutierrez, *et al.*, "Cohesive framework for non-line-of-sight imaging based on Dirac notation," *Opt. Express* **32**(6), 10505–10526 (2024).
53. <https://github.com/jgarciapueyo/ForwardAndInverseDiffractionInPhasorFields> (2025).